Py4CAtS

Line-by-Line Tools for Molecular Optical Depths

Franz Schreier

DLR — Remote Sensing Technology Institute
Oberpfaffenhofen, 82234 Wessling, Germany

July 25, 2011

Contents

List of Figures

1 Introduction

An essential prerequisite for the analysis of data recorded by atmospheric remote sensing instruments as well as for theoretical investigations such as retrieval assessments is a flexible, yet efficient and reliable high resolution radiative transfer code. Furthermore, as the retrieval of atmospheric parameters is in general a nonlinear optimization problem (inverse problem), the retrieval code has to be closely connected to the radiative transfer code (forward model).

Although a variety of general purpose high resolution radiative transfer models has been developed in the past decades, nb. FASCODE [Clough et al., 1988] and GENLN2 [Edwards, 1988], a new code has been found to be desirable because implementation of these sophisticated line-by-line (lbl) programs in retrieval algorithms is generally a non–trivial task. Furthermore derivatives with respect to the unknown profiles are often not available or at least difficult to access (more recent developments such as KOPRA Stiller et al. [2002] or ARTS Bühler et al. [2005] providing analytical derivatives were not available then).

Given the variety of applications at DLR–IMF a new code has been designed for arbitrary observation geometry and instrumental field-of-view (FOV) and line shape (ILS). The original implementation MIRART(Modular InfraRed Atmospheric Radiative Transfer), written in Fortran 77, has been developed with emphasis on efficient and reliable numerical algorithms and a modular approach appropriate for simulation and/or retrieval. More recently this has been translated to modern Fortran 90/2003 as GARLIC (Generic Atmospheric Radiation Line-by-line Infrared Code). Concurrently a version of MIRART/GARLIC written in Python Langtangen [2004] has been developed.

2 Physical Basics of Infrared Radiative Transfer

2.1 Schwarzschild Equation and Beer's Law

In the infrared and microwave spectral range the intensity (radiance) I at wavenumber ν received by an instrument at $s = 0$ can be described by the integral form of the equation of radiative transfer (neglecting scattering and assuming local thermodynamic equilibrium) [Liou, 1980, Goody and Yung, 1989, Zdunkowski et al., 2007]

$$I(\nu) = I_{\mathrm{b}}(\nu)\mathcal{T}(\nu;\infty) - \int_0^{s_{\mathrm{b}}} \mathrm{d}s'\ B(\nu,T(s'))\ \frac{\partial \mathcal{T}(\nu;s')}{\partial s'} \tag{1}$$

$$= I_{\mathrm{b}}(\nu)\mathcal{T}(\nu;\infty) - \int_0^{\tau_{\mathrm{b}}} \mathrm{d}\tau\ B(\nu,T(\tau))\exp(-\tau) \tag{2}$$

where I_{b} is a background contribution (e.g., solar radiation at the top of the atmosphere in case of uplooking or limbviewing geometry, or surface emission in case of nadir viewing geometry) and B is the Planck function at temperature T,

$$B(\nu,T) = 2hc^2\nu^3 \Big/ \left(e^{hc\nu/k_BT} - 1\right), \tag{3}$$

with c, h, k_B denoting speed of light, Planck constant, and Boltzmann constant, respectively. The monochromatic transmission $\mathcal{T}$ (relative to the observer) is given according

to Beer's law by

$$\mathcal{T}(\nu; s) = \mathrm{e}^{-\tau(\nu;s)} \tag{4}$$

$$= \exp\left[-\int_0^s \alpha(\nu, s')\ \mathrm{d}s'\right]\ , \tag{5}$$

$$\alpha(\nu; s) = \sum_m k_m(\nu, s)\ n_m(s) + \alpha^t ext(c)(\nu, s) \tag{6}$$

where τ is the optical depth, α is the volume absorption coefficient, k_m and n_m are the absorption cross section and density of molecule m, and $\alpha^{(\mathrm{c})}$ the continuum absorption coefficient. Note that the absorption cross section is a function of (altitude dependant) pressure and temperature, but for brevity the condensed notation $k(\nu, z) = k\big(\nu, p(z), T(z)\big)$ has been used. In (1) we have assumed an uplooking or limb viewing path geometry, but (1) is easily rewritten to other slant path geometries. It should also be noted that the instrumental influence on the measured spectrum has been neglected.

2.2 Molecular Absorption

In general the molecular cross section is obtained by summing over the contributions from many lines,

$$k_m(\nu, z) = \sum_l S_l^{(m)}(T(z))\ g(\nu;\ \hat{\nu}_l^{(m)}, \gamma_l^{(m)}(p(z), T(z)))\ . \tag{7}$$

In the infrared and microwave spectral range molecular absorption is due to radiative transitions between rotational and ro–vibrational states of the molecules. A single spectral line is characterized by its position $\hat{\nu}$, line strength S, and line width γ, where the transition wavenumber (or frequency) is determined by the energies E_i, E_f of the initial and final state, $|i\rangle$, $|f\rangle$,

$$\hat{\nu} = \frac{1}{hc}\ (E_\mathrm{f} - E_\mathrm{i}) \tag{8}$$

For an individual line the cross section is the product of the temperature dependent line strength $S(T)$ and a normalized line shape function $g(\nu)$ describing the broadening mechanism, $k(\nu, z) = S(T(z)) \cdot g\big(\nu, p(z), T(z)\big)$. In the atmosphere the combined effect of pressure broadening (corresponding to a Lorentzian line shape) and Doppler broadening (corresponding to a Gaussian line shape) can be represented by a Voigt line profile.

2.2.1 Line strength and partition functions

The monochromatic absorption cross section for a single line is defined as the product of the line strength S and a normalized line profile function g essentially determined by line broadening,

$$k(\nu; \hat{\nu}, S, \gamma) = S\ \cdot\ g(\nu; \hat{\nu}, \gamma) \qquad \text{with} \quad \int_{-\infty}^{+\infty} g\ \mathrm{d}\nu = 1\ . \tag{9}$$

For electric dipole transitions the line strength is determined by the square of the temperature dependent matrix element of the electric dipole moment and by further factors accounting for the partition function, Boltzmann-distribution, and stimulated emission,

$$S(T) = \frac{8\pi^3}{3hc}\ \frac{g_i I_a}{Q(T)}\ \hat{\nu}\ e^{-E_i/kT}\left[1 - e^{-hc\hat{\nu}/kT}\right]\ R_{if} \cdot 10^{-36} \tag{10}$$

here g_i is the degeneracy of the nuclear spin of the lower energy state, I_a is the relative abundance of the isotope[1], $Q(T)$ is the total partition sum, R_{if} is the transition probability given by the matrix element of the electric dipole operator $R_{if} = |\langle f|\boldsymbol{D}|i\rangle|^2$. A similar expression is found for the line strength of magnetic quadrupole transitions. In both cases the ratio of line strength at two different temperatures is given by

$$S(T) \;=\; S(T_0) \;\times\; \frac{Q(T_0)}{Q(T)} \;\frac{\exp\left(-E_i/kT\right)}{\exp\left(-E_i/kT_0\right)} \;\frac{1 \;-\; \exp\left(-hc\hat{\nu}/kT\right)}{1 \;-\; \exp\left(-hc\hat{\nu}/kT_0\right)} \;. \tag{11}$$

$Q(T)$ is the product of the rotational and vibrational partition functions, $Q = Q_{\rm rot} \cdot Q_{\rm vib}$, whose temperature dependance are calculated from

$$Q_{\rm rot}(T) \;=\; Q_{\rm rot}(T_0) \left(\frac{T}{T_0}\right)^{\beta} \;, \tag{12}$$

$$Q_{\rm vib}(T) \;=\; \prod_{i=1}^{N} \left[1 - \exp(-hc\omega_i/kT)\right]^{-d_i} \;, \tag{13}$$

where β is the temperature coefficient of the rotational partition function, and N is the number of vibrational modes with wavenumbers ω_i and degeneracies d_i. Data required to calculate the vibrational partition sums have been taken from Norton and Rinsland [1991].

2.2.2 Pressure (collision) broadening — Lorentz profile

In case of pure pressure broadening the cross section for a single radiative transition is essentially given by a Lorentzian line profile

$$g_{\rm L}(\nu) \;=\; \frac{\gamma_{\rm L}/\pi}{(\nu - \hat{\nu})^2 + \gamma_{\rm L}^2} \;. \tag{14}$$

The Lorentz half width (at half maximum, HWHM) $\gamma_{\rm L}$ is proportional to pressure p and decreases with increasing temperature. In case of a gas mixture with total pressure p and partial pressure p_s of the absorber molecule the total width is given by the sum of a self broadening contribution due to collisions between the absorber molecules and an air-broadening contribution due to collisions with other molecules,

$$\gamma_{\rm L}(p, p_s, T) \;=\; \left(\gamma_{\rm L}^{(0,{\rm air})} \;\frac{p - p_{\rm s}}{p_0} \;+\; \gamma_{\rm L}^{(0,{\rm self})} \;\frac{p_{\rm s}}{p_0}\right) \;\times\; \left(\frac{T_0}{T}\right)^{n} \;. \tag{15}$$

The exponent n specifying the dependence of temperature is so far known for only a few transitions of the most important molecules. The kinetic theory of gases (collision of hard spheres) yields the classical value $n = \frac{1}{2}$. The self-broadening coefficient $\gamma_{\rm L}^{(\rm self)}$ is so far known for only a few transitions and will otherwise be set to the air-broadening coefficient $\gamma_{\rm L}^{(\rm air)}$ (mostly specified for N_2 and/or O_2), i.e.

$$\gamma_{\rm L}(p, T) \;=\; \gamma_{\rm L}^{(\rm air)} \;\frac{p}{p_0} \;\times\; \left(\frac{T_0}{T}\right)^{n} \tag{16}$$

Typical values of air-broadening coefficients are $\gamma_{\rm L} \approx 0.1p$ [$\rm cm^{-1}$/atm] (see Tab. 2 in Rothman et al. [1987]).

[1] In the HITRAN– and GEISA databases the abundances of the Earth atmosphere are used.

2.2.3 Doppler broadening

The thermal motion of the molecules leads to Doppler boradening of the spectral lines, which is described by a Gaussian line shape

$$g_{\mathrm{D}}(\nu) \;=\; \frac{1}{\gamma_{\mathrm{D}}} \left(\frac{\ln 2}{\pi}\right)^{1/2} \cdot \exp\left[-\ln 2 \left(\frac{\nu-\hat{\nu}}{\gamma_{\mathrm{D}}}\right)^2\right] \;. \tag{17}$$

The half width (HWHM) is essentially determined by the line position $\hat{\nu}$, the temperature T, and the molecular mass m,

$$\gamma_{\mathrm{D}} \;=\; \hat{\nu}\,\sqrt{\frac{2\ln 2\;kT}{mc^2}} \;. \tag{18}$$

For a typical atmospheric molecule one finds

$$\gamma_{\mathrm{D}} \approx 6\cdot 10^{-8}\,\hat{\nu}\sqrt{T\,[K]} \qquad \text{for} \quad m \approx 36\,\text{amu}.$$

2.2.4 Combined Pressure and Doppler broadening

The combined effects of both broadening mechanisms can be modelled by convolution, i.e., a Voigt line profile

$$\begin{aligned} g_{\mathrm{V}}(\nu-\hat{\nu},\gamma_{\mathrm{L}},\gamma_{\mathrm{D}}) \equiv\; & g_{\mathrm{L}} \otimes g_{\mathrm{D}} \\ =\; & \int_{-\infty}^{\infty} \mathrm{d}\nu'\; g_{\mathrm{L}}(\nu-\nu';\hat{\nu},\gamma_{\mathrm{L}}) \;\times\; g_{\mathrm{D}}(\nu'-\hat{\nu};\hat{\nu},\gamma_{\mathrm{D}}) \;. \end{aligned} \tag{19}$$

Several empirical approximations for the half width (HWHM) of a Voigt line (defined by $g_V(\hat{\nu}\pm\gamma_V) \;=\; \frac{1}{2}g_V(\hat{\nu})$) have been developed [Olivero and Longbothum, 1977]. For the approximation

$$\gamma_V \;=\; \frac{1}{2}\left(c_1\gamma_{\mathrm{L}} \;+\; \sqrt{c_2\gamma_{\mathrm{L}}^2+4\gamma_D^2}\right) \qquad \text{with} \quad c_1 = 1.0692,\; c_2 = 0.86639 \tag{20}$$

a accuracy of 0.02% has been specified, with $c_1 = c_2 = 1$ the accuracy is in the order of one percent. A comparison of Lorentzian, Doppler, and Voigt half width is given in Fig. 1.

3 Algorithms

3.1 Numerical Aspects — Computational Challenges

The computational challenge of high resolution atmospheric radiative transfer modelling is due to several facts. The summation in Eq. (7) has to include all relevant lines contributing to the spectral interval considered. In many line–by–line codes a cutoff wavenumber of $25\,\mathrm{cm}^{-1}$ from line center is frequently employed for truncation of line wings. Note that the widely used HITRAN and GEISA spectroscopic databases [Rothman et al., 2009, Jacquinet-Husson et al., 2008] list more than some million lines of about 40 molecules in the microwave, infrared, to ultraviolet regime, whereas the JPL spectral line catalog [Pickett et al., 1998] covering the submillimeter, millimeter, and microwave only has almost 2 million entries.

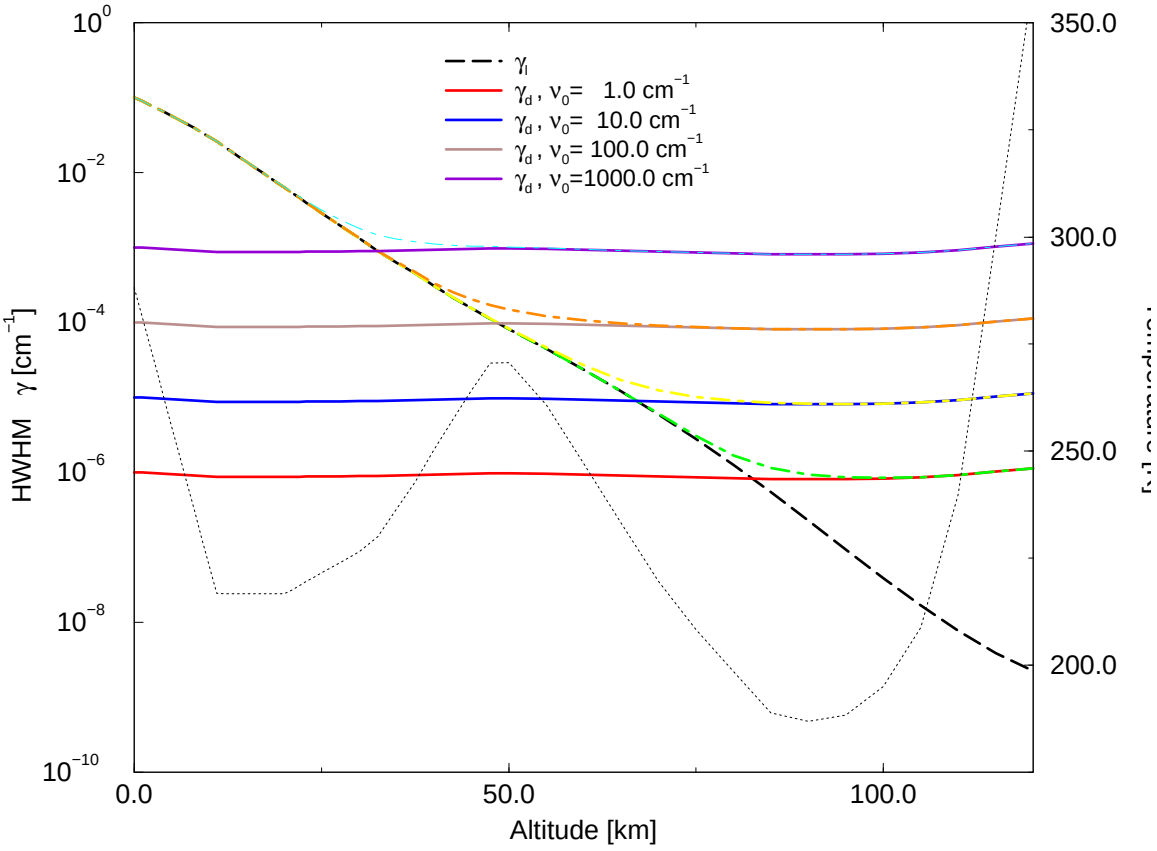

Figure 1: Half widths (HWHM) for Lorentz-, Doppler- and Voigt-Profile as a function of altitude for a variety of line positions $\hat{\nu}$. The Lorentz width is essentially proportional to pressure and hence decays approximately exponentially with altitude. In contrast the Doppler width is only weakly altitude dependent. In the troposphere lines are generally pressure broadened, the transition to the Doppler regime depends on the spectral region. The dotted line indicated atmospheric temperature. (Pressure and temperature: US Standard atmosphere, molecular mass $36amu$)

Furthermore the wavenumber grid has to be set in accordance with the line widths γ, i.e. the grid spacing is typically chosen in the order of $\delta\nu \approx \gamma/4$. Typical line widths due to pressure broadening are in the order of $\gamma(p) \approx (p/p_0)\,0.1\,\mathrm{cm}^{-1}$ with $p_0 = 1013\,\mathrm{mb}$. In the atmosphere the pressure decays approximately exponentially with altitude z, and the line width decreases accordingly until Doppler broadening (proportional to line position and the square root of the temperature over molecular mass ratio) becomes dominant (cf. Fig. 1). Hence, for an altitude of $z = 100\,\mathrm{km}$ with a pressure $p \approx 10^{-4}\,\mathrm{mb}$ the number of spectral grid points required for a spectral interval $\Delta\nu = 1\,\mathrm{cm}^{-1}$ in the microwave is in the order of $1/(0.1 \times 10^3/10^{-4}) = 10^6$. For a spectral interval of width $\Delta\nu = 10\,\mathrm{cm}^{-1}$ in the region of the CO_2 ν_2 band around $500\,\mathrm{cm}^{-1}$ the number of spectral grid points is in the order of 10^5.

A variety of approaches has been developed to speed–up the calculation and an essential difference between different line–by–line codes is the choice of the line profile approximation, wavenumber grid, and interpolation. Some of the algorithms are specifically

designed for the individual functions to be calculated, e.g., the Clough and Kneizys [1979] algorithm used in FASCODE [Clough et al., 1988]: The Lorentzian (or Voigt function) is decomposed using three or four even quartic functions, each of them is then calculated on its individual grid. (A similar technique using quadratic functions has been developed by Uchiyama [1992].) GENLN2 [Edwards, 1988] performs the line–by–line calculation in two stages, i.e., the entire spectral interval of interest is first split in a sequence of "wide meshes"; contributions of lines with their center in the current wide mesh interval are computed on a fine mesh, and the contribution of other lines is computed on the wide mesh. Fomin [1995] defines a series of grids and evaluates line wing segments of larger distance to the line center on increasingly coarse grids. Sparks [1997] also uses a series of grids with $2^k + 1$ grid points ($k = 1, 2, \ldots$, where the coarsest grid with 3 points spans the entire region) and uses a function decomposition similar to ours.

3.2 Voigt profile and Voigt function

The convolution of a Lorentz and a Gauss profile, commonly known as the Voigt profile, is important in many branches of physics, nb. atomic and molecular spectroscopy, atmospheric radiative transfer [Armstrong, 1967].

It is convenient to define the Voigt function $K(x, y)$ normalized to $\sqrt{\pi}$,

$$K(x,y) \;=\; \frac{y}{\pi} \int_{-\infty}^{\infty} \frac{\mathrm{e}^{-t^2}}{(x-t)^2 + y^2}\, \mathrm{d}t \;, \tag{21}$$

where the dimensionless variables $x,\ y$ are defined in terms of the distance from the center position, $\nu - \hat{\nu}_0$, and the Lorentzian and Gaussian half–widths $\gamma_\mathrm{L},\ \gamma_\mathrm{G}$:

$$x \;=\; \sqrt{\ln 2}\, \frac{\nu - \hat{\nu}}{\gamma_\mathrm{G}} \qquad \text{and} \qquad y \;=\; \sqrt{\ln 2}\, \frac{\gamma_\mathrm{L}}{\gamma_\mathrm{G}} \;. \tag{22}$$

The Voigt function represents the real part of the complex function

$$W(z) \;\equiv\; K(x,y) + \mathrm{i}L(x,y) \;=\; \frac{\mathrm{i}}{\pi} \int_{-\infty}^{\infty} \frac{e^{-t^2}}{z-t}\, \mathrm{d}t \qquad \text{with} \qquad z = x + \mathrm{i}y, \tag{23}$$

that, for $y > 0$, is identical to the complex error function (probability function) defined by [Abramowitz and Stegun, 1964]

$$w(z) \;=\; \mathrm{e}^{-z^2} \left(1 \;+\; \frac{2\mathrm{i}}{\sqrt{\pi}} \int_0^z \mathrm{e}^{t^2}\, \mathrm{d}t\right) \;=\; \mathrm{e}^{-z^2} \left(1 \;-\; \mathrm{erf}(-\mathrm{i}z)\right) \;. \tag{24}$$

The complex error function satisfies the differential equation

$$w'(z) \;=\; -\,2z \cdot w(z) \;+\; \frac{2\mathrm{i}}{\sqrt{\pi}} \tag{25}$$

and the series and asymptotic expansions (where Γ is the gamma function)

$$w(z) = \sum_{n=0}^{\infty} \frac{(\mathrm{i}z)^n}{\Gamma\left(\frac{n}{2} + 1\right)} \tag{26}$$

$$w(z) = \frac{\mathrm{i}}{\pi} \sum_{k=0}^{\infty} \frac{\Gamma\left(k + \frac{1}{2}\right)}{z^{2k+1}} \;. \tag{27}$$

Unfortunately, none of these functions can be evaluated in closed analytical form and a large number of numerical algorithms have been developed in the past [Schreier, 1992]. Most modern algorithms for the Voigt function employ approximations for the complex error function. Actually this approach has further advantages, in particular it simultaneously provides derivatives of these functions, required for, e.g., sensitivity analysis or optimization. Furthermore, the complex error function can be used if more sophisticated line profiles, e.g., the Rautian for collisional narrowing, or line mixing effects have to be computed.

Rational approximations are known to give accurate and efficient algorithms for a large class of functions, and also have been successfully used to approximate the complex error function, e.g., Hui et al. [1978], Humlíček [1979, 1982], Weideman [1994].

$$w(z) \;=\; \frac{P(\tilde{z})}{Q(\tilde{z})} \;=\; \frac{\sum_{m=0}^{M} a_m \tilde{z}^m}{\sum_{n=0}^{M+1} b_n \tilde{z}^n} \qquad \text{where} \quad \tilde{z} = y - \mathrm{i}x. \tag{28}$$

Because of the asymptotic behaviour of the complex error function $w \sim 1/z$), the degree of the nominator and denominator polynomials are constrained by $N = M + 1$. It should be noted, that for atmospheric spectroscopy applications the Lorentz to Gauss width ratio varies over many orders of magnitude, i.e., $10^{-7} < y < 10^4$ (see Figures 2 and 3 in [Schreier, 2011]). On the other hand, $K(x, y)$ and $w(z)$ are especially difficult to evaluate for small $y < 1$, and in most algorithms the x, y plane (or the first quadrant $x, y \geq 0$ because of the symmetry relations) is divided in several regions and appropriate methods are utilized, e.g., a series approximation for small x, y and an asymptotic approximation for large x, y.

The Hui et al. [1978] and Weideman [1994] rational approximations appear to be quite tempting as they provide a single approximation applicable to the entire x, y plane. However, the Hui et al. 1978 algorithm (with $M = 6$) has significant accuracy problems for small y and medium x, and the Weideman 1994 approximations requires a large number of terms to achieve sufficient accuracy for small y, making it computationally less efficient. The Humlíček [1982] code (or variations thereof, e.g., Kuntz [1997], Imai et al. [2010]) has been selected by several authors, but its performance depends on the compiler's efficiency to handle nested conditional branches.

In order to avoid complicated `if` constructs for the calculation of the complex error function, `lbl2xs` and `lbl2od` use an optimized combination of the Humlíček [1982] and Weideman 1994 algorithms [Schreier, 2011]

$$w(z) \;=\; \begin{cases} \frac{\mathrm{i}z/\sqrt{\pi}}{z^2 - \frac{1}{2}} & |x| + y > 15, \\ \frac{\pi^{-1/2}}{L - \mathrm{i}z} \;+\; \frac{2}{(L-\mathrm{i}z)^2} \sum_{n=0}^{N-1} a_{n+1} Z^n & \text{otherwise}, \end{cases} \tag{29}$$

where $Z = \frac{L+\mathrm{i}z}{L-\mathrm{i}z}$ and $L = 2^{-1/4} N^{1/2}$. For $N = 24$ this provides an accuracy better than 10^{-4} everywhere except for very small $y < 10^{-5}$ and $4 < x < 15$; for $N = 32$ the relative error $|\Delta K|/K$ is less than $8 \cdot 10^{-5}$ for all x, y, cf. Fig. 2.

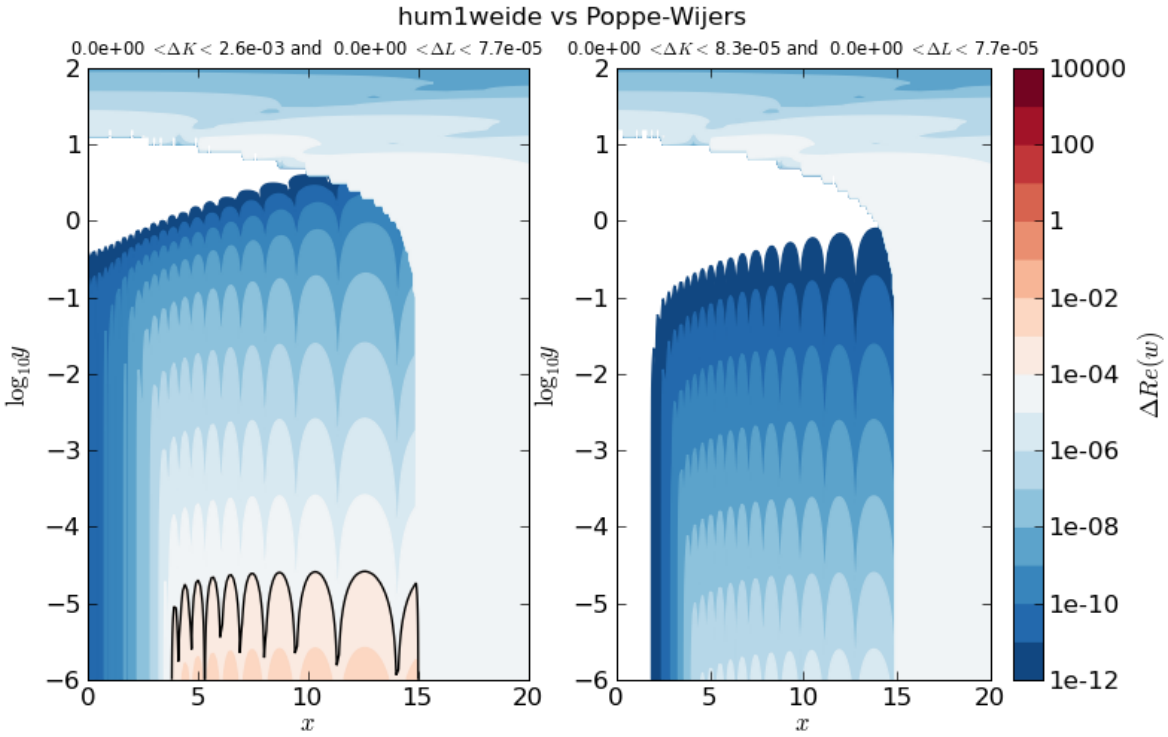

Figure 2: Relative accuracy of the combined Humliček I and Weideman approximation (left $N = 24$ and right $N = 32$).

3.3 Multigrid algorithm

The problem is the efficient computation of a superposition of similar functions $f_l(x)$ over a large region of its independent variable x,

$$F(x_i) \;=\; \sum_{l=1}^{L} f_l(x_i) \qquad \text{for} \quad x_{\rm lo} \equiv x_0 < x_1 < \cdots < x_i < \cdots < x_n \equiv x_{\rm hi}. \tag{30}$$

Frequently the functions $f_l(x)$ vary rapidly only in a small region of the entire domain, but the evaluation of $F(x)$ covers a large x–interval where the individual f_l is mostly smooth. However, accurate modelling of the function sum requires appropriate sampling of the x–grid, i.e., the grid interval size δx has to be chosen small enough to resolve the details of $f_l(x)$ in the regions of strong variability. Thus, for an uniform/equidistant grid the spacing δx is determined by the fine structure of the f_l's.

Computing $f_l(x)$ on a uniform, appropriately dense grid over the entire region of interest is obviously not very efficient when f_l is smooth everywhere except for a small subinterval of $[x_{\rm lo}, x_{\rm hi}]$. The calculation is significantly accelerated when f_l is decomposed into rapidly and slowly varying contributions, where the fast part has to be computed on a fine grid in the region of strong variability only and the smooth part is computed on a coarse grid covering the entire interval of interest. Furthermore, if the smooth part is a continuous function of x over the entire interval $[x_{\rm lo}, x_{\rm hi}]$, the sum in (30) can be performed separately for the rapidly and slowly varying contributions,

$$F^{\rm fast}(x) \;=\; \sum_l f_l^{\rm fast}(x) \qquad \text{where} \quad x \in \{x_0, \ldots, x_n\} \qquad \text{(fine grid)} \tag{31}$$

$$F^{\rm smooth}(X) \;=\; \sum_l f_l^{\rm smooth}(X) \qquad \text{where} \quad X \in \{X_0, \ldots, X_N\} \qquad \text{(coarse grid)} \tag{32}$$

and the interpolation to the fine grid x is required only once after the entire sum has been evaluated,

$$F(x) \;=\; F^{\text{fast}}(x) \;+\; \mathcal{I}\left[F^{\text{smooth}}(X)\right](x)\;. \tag{33}$$

Here $\mathcal{I}$ denotes an interpolation operator, i.e., $\mathcal{I}\left[F^{\text{smooth}}\right](x)$ is the interpolated sum of smooth contributions (available at the coarse grid X) at the fine grid point x. In order to guarantee an efficient interpolation, an equidistant set of N coarse grid points $X_0, X_1, \ldots, X_N$ with spacing ΔX satisfying $\Delta X/\delta x = n/N$ integer will be used (furthermore $X_0 = x_0$ and $X_N = x_n$). For convenience ratios of power two will be used, i.e., $n/N = 2^m$. Clearly, the larger the ratio, the larger the computational speed–up. However, for very large coarse grid spacings, errors due to inadequate sampling of the smooth contribution to f become too big. For our applications ratios $n/N = 4$ and $n/N = 8$ have turned out to provide a reasonable compromise between speed and accuracy.

Thus the problem of efficient calculation of the sum (30) has been transformed into the problem of splitting off the smooth part of each f_l, i.e.,

$$f_l(x) \;=\; f_l^{\text{smooth}}(x) + f_l^{\text{fast}}(x) \tag{34}$$

The simplest choice of the smooth function that automatically satisfies the constraints of continuity is to use the function f_l itself as smooth function f_l^{smooth}, too. Note that the sum of the smooth contributions F^{smooth} is interpolated to the fine grid and then added to the sum of the fine grid, quickly varying contributions. In order to compensate for the interpolated smooth contributions in the regions of strong variability, the quickly varying contribution is defined as

$$f_l^{\text{fast}}(x) \;=\; f_l(x) - \mathcal{I}\left[f^{\text{smooth}}\right](x) \qquad \text{for } x \text{ in center region.} \tag{35}$$

Note that f_l^{fast} or its first derivative may have discontinuities. In Fig. 3 this decomposition is shown for the Lorentzian line shape.

The speed–up that can be achieved with the two–grid algorithm developed in the previous subsection is essentially determined by the ratio of grid points on the fine and coarse grid, i.e. with $n/N = 4$ or $n/N = 8$ only a small computational gain is possible. A significant acceleration can be achieved by using further grids with increasing grid point spacing. However, for our applications to spectral modelling the computational overhead required to control a series of grids turned out to partly compensate the speed–up provided by very coarse grids, and simply using three grids turned out to be efficient [Schreier, 2006].

3.4 Path Quadrature

To evaluate the optical depth τ according to (4) it is necessary to compute the integral of the absorption coefficient $\alpha(z)$ along the (vertical or slanted) path (`lbl2od` considers a plane-parallel atmosphere, so it is restricted to up- and down-looking viewing geometries, and limb viewing is not supported.)

The trapezoidal rule is perhaps the most basic and important Newton-Cotes formula for numerical evaluation of an integral of a function $y(x)$,

$$\int_{x_0}^{x_n} y(x)\,\mathrm{d}x = \frac{1}{2}\sum_{i=1}^{n}(y_i + y_{i-1})(x_i - x_{i-1})\;. \tag{36}$$

Clearly the assumption behind the trapez rule, i.e. a linear polynomial interpolating the function y in the subintervals $[x_{i-1}, x_i]$, is hardly justified in view of the exponential

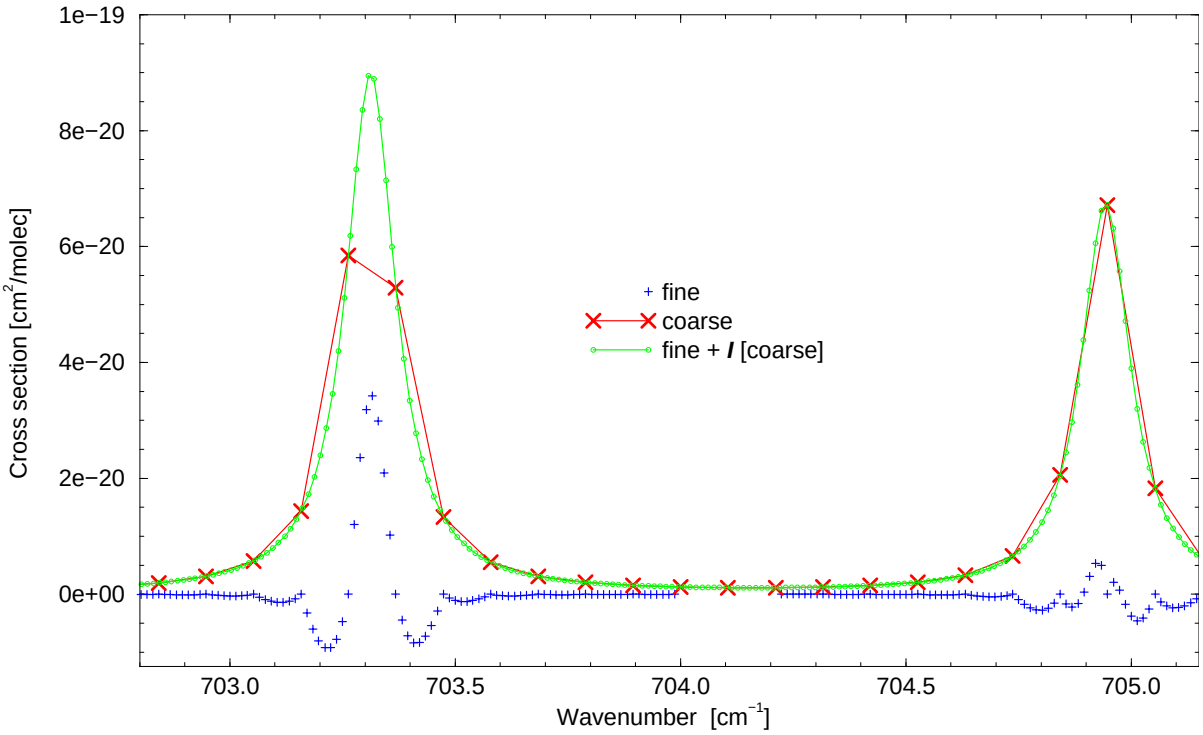

Figure 3: Lorentzian line profile function (14) decomposed in a slowly varying contribution (evaluated on a coarse grid) and a rapidly varying contribution evaluated on a fine grid near the center only (Two–point Lagrange interpolation). The example corresponds to CO_2 cross sections at 1013.25 mb and 296 K; for clarity only the strongest lines have been included.

dependence of air number density or the presence of steep gradients of, e.g., the water concentration profile. Nevertheless, the trapez rule is the most robust and fastest quadrature rule, and it is the default rule used here.

As an alternative, `lbl2od` offers the possibility to use Simpson's rule (using `integrate.simps` from SciPy), the next higher Newton-Cotes formula assuming a quadratic interpolating polynomial. Note that especially for the difference or cumulative optical depth this can be very time-consuming.

4 Verification and Applications

The standard approach to verification of LbL codes relies on cross checks against similar codes. MIRART/GARLIC participated in two extensive intercomparisons.

4.1 AMIL2DA

In order to assess the consistency of level 2 data generated from measurements by the MIPAS Fourier transform limb emission spectrometer onboard the ENVISAT satellite, the AMIL2DA project aimed at careful comparison and characterization of algorithms and data analysis stategies used by different European groups. An essential step of this project was a cross comparison of the radiative transfer forward models to be used as part of the group's MIPAS data processing [von Clarmann et al., 2002]. The intercomparison was organized as a series of exercises, starting from simple settings proving basic

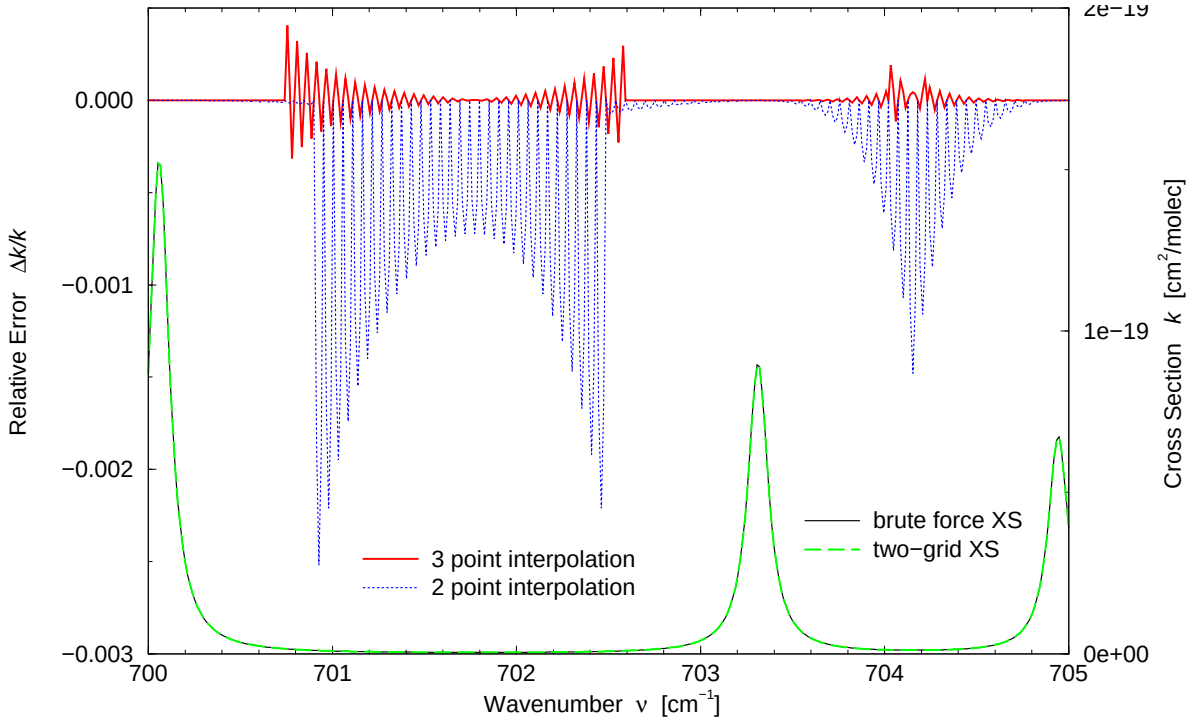

Figure 4: Error of the sum of some Lorentzians (14) evaluated with a two–grid approximation and linear and quadratic Lagrange interpolation. For two–point interpolation the fine grid was used within $\nu_l \pm 12\gamma$ around the line center. whereas for three–point interpolation the fine grid extension was $\nu_l \pm 10\gamma$. The sum of Lorentzians (cross section, "XS") evaluated with the "brute force" and with the two–grid–algorithm are indistinguishable. (Same example as in Fig. 3.)

functionalities and proceeding to more complex and realistic scenarios. Accordingly the first exercises considered the transmission of a single N_2O line for different pressures and temperatures, hence testing line shape computation and line strength conversion. In a second set of exercises radiance spectra for a limb viewing geometry with instrumental effects have been intercompared. Figure 5 shows a comparison of a limb emission spectrum, revealing deviations well below one percent.

4.2 IRTMW01

A major objective of IRTMW01 was the intercomparison of radiative transfer codes in the microwave spectral domain [Melsheimer et al., 2005]. Similar to the AMIL2DA intercomparison it was organized in a series of progressively more sophisticated "cases", starting with an assessment of Voigt line shape and molecular absorption coefficient calculations. As for the corresponding AMIL2DA exercises MIRART exhibited slight deviations for spectra at temperatures different from the database reference temperature, that have been attributed to the use of different line strengths conversion approaches.

The purpose of case 3 was to check the correct implementation of the radiative transfer algorithm, nb., the solution of the integrals in Eqs. (1) and (4). In order to allow to discriminate different sources of possible deviations between the models, absorption coefficients $\alpha(\nu, z)$ have been pre–calculated by the University of Bremen group and used as common input. Case 4 was aiming to test the entire computational chain of the codes including LbL calculation, continuum corrections, and path quadrature. Geometries and

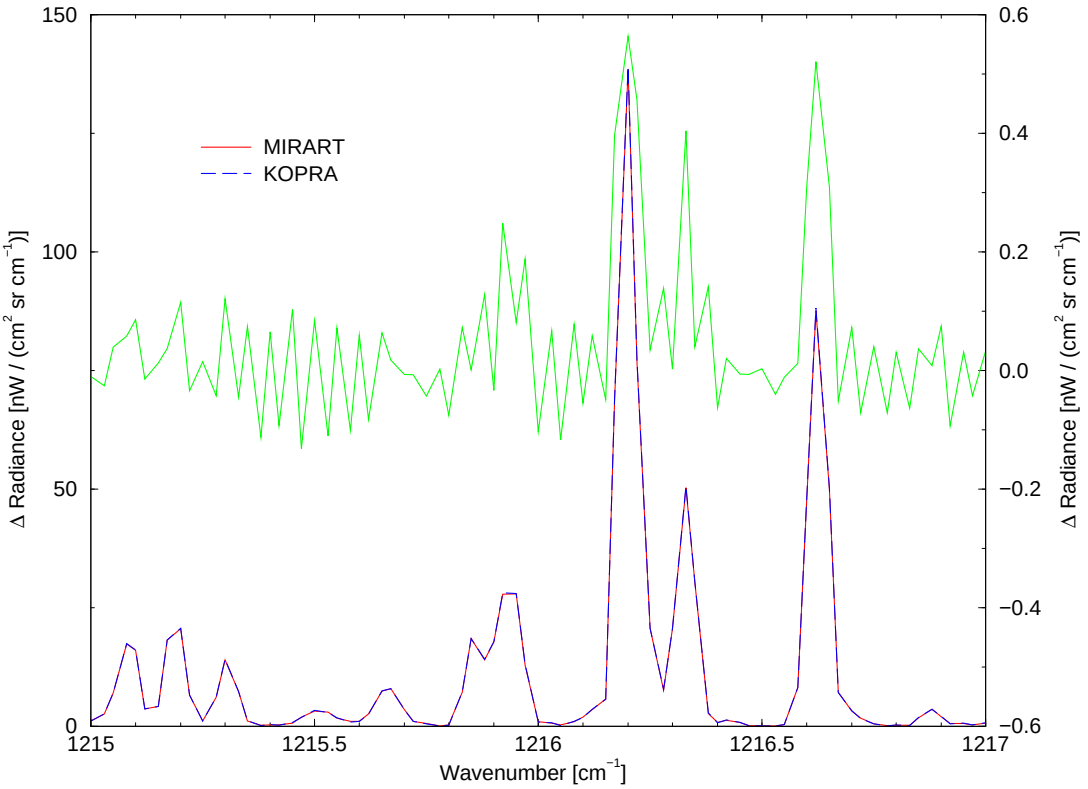

Figure 5: AMIL2DA Forward model intercomparison (Exercise 20):
KOPRA line–by–line code [Stiller et al., 2002] and MIRART.
Limb view with tangent altitude 40 km, apodized FTS instrument line shape, finite field–of–view, H_2O, CO_2, O_3, N_2O, and CH_4; CKD–continuum [Clough et al., 1988].

instrument settings were identical to case 3, thus changes from case 3 spectra to case 4 spectra have to come from differences in the input data or from differences in the cross section and absorption coefficient calculations.

The intercomparison was performed for different geometries, and for ideal monochromatic spectra as well as ILS (instrument line shape) and FoV (field-of-view) convolved spectra. Figure 6 shows the results for the uplooking geometry: Whereas case 3 spectra do not yield visible differences, slight deviations show up in case 4 for small zenith angles. Similar results were also found for the case 3 and case 4 down looking and limb viewing exercises.

5 Py4CaTS — The Python Scripts

Py4CAtS is a Python (`www.python.org`) re-implementation of the Fortran infrared radiative transfer code MIRART/GARLIC. Clearly a pure Python implementations would be by far too slow for a computational challening task such as line-by-line modeling, so Py4CAtS makes heavy use of the Numeric Python extensions (`www.numpy.org`, Langtangen [2004]). The motivation to rewrite the code in Python was to provide easy access to intermediate quantities such as cross sections, absorption coefficients, or optical depths that is sometimes quite useful to deepen the understanding of the "physics" involved in a particular remote sensing application. Furthermore this appeared to be a way towards "computational steering", i.e., combining the best of two worlds by letting Python

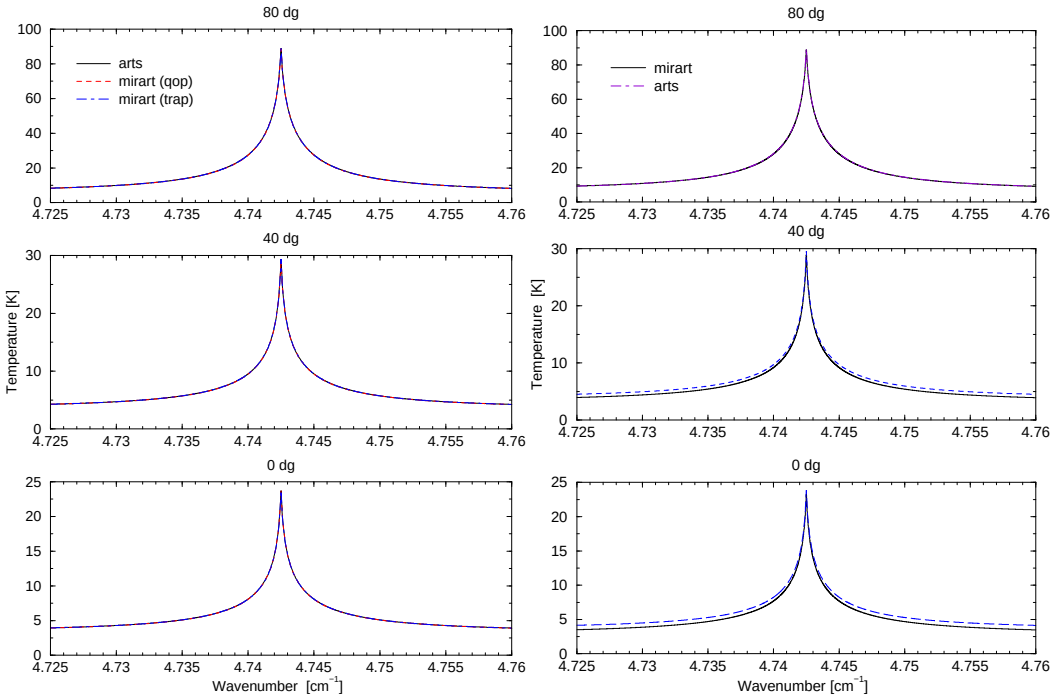

Figure 6: IRTMW01 intercomparison: case 3 (left) and 4 (right) up–looking: ARTS line–by-line code (University of Bremen, Bühler et al. [2005]) vs. MIRART. O_3 and O_2, perfect antenna (i.e. infinitesimal FoV), single side band receiver with Gaussian ILS function with half width 0.25 MHz.

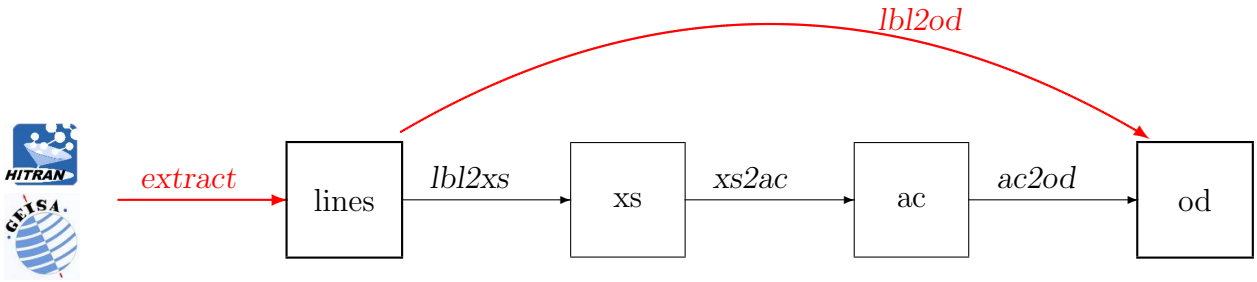

Figure 7: From Hitran/Geisa via cross sections and absorption coefficients to optical depths.

do the control, book-keeping etc., and executing the compute-intensive code-sections in compiled Fortran. However, the original approach with PyFort Dubois and Yang [1999] turned out to be somewhat difficult to port from machine to machine, and the recent advances with Numeric Python (allowing highly optimized array-processing) made this need for Fortran–Python interfacing less critical.

In Py4CAtS the individual steps of an infrared radiative transfer computation are implemented in separate scripts, see Fig. 7:

- `extract` (select) lines of relevant molecules in the spectral range of interest
- `lbl2xs` compute line-by-line cross sections for given pressure(s) and temperature(s)
- `xs2ac` multiply cross sections with number densities and sum over all molecules

```
mkdir example
cd example
extract -x 50,60
/data/hitran/2000/lines
lbl2xs H2O.vSEan O3.vSEan OH.vSEan
xs2ac H2O.xs O3.xs OH.xs
ac2od H2O+O3+OH.ac
```

For each molecule and p, T level:

$$k^{(m)}(\nu, p_l, T_l) = \sum_l S_l g(\nu, \hat{\nu}_l, \gamma_l)$$

$$\alpha_l(\nu) = \sum_m k^{(m)}(\nu, p_l, T_l) n_m(z_l)$$

$$\tau_l(\nu) = \int_{z_l}^{z_{l+1}} \alpha_l(\nu)\, \mathrm{d}z$$

Figure 8: Typical workflow for line-by-line modelling with Py4CAtS: Hitran/Geisa $\longrightarrow$ line parameter extracts $\longrightarrow$ cross sections $\longrightarrow$ absorption coefficients $\longrightarrow$ optical depth (Note that on the left hand side the output files are not indicated (usually done with the `-o` option). Furthermore specification of atmospheric data (pressure and temperature for `lbl2xs`, and additionally gas concentrations for `xs2ac` is not shown.)

```
mkdir example
cd example
extract -x 50,60 \
       /data/hitran/2008/lines
lbl2od atmos.data \
       H2O.vSEan O3.vSEan OH.vSEan
```

For each molecule and p, T level:

$$k^{(m)}(\nu, p_l, T_l) = \sum_l S_l g(\nu, \hat{\nu}_l, \gamma_l)$$

$$\alpha_l(\nu) = \sum_m k^{(m)}(\nu, p_l, T_l) n_m(z_l)$$

$$\tau_l(\nu) = \int_{z_l}^{z_{l+1}} \alpha_l(\nu)\, \mathrm{d}z$$

Figure 9: Typical workflow: From Hitran/Geisa line parameter extract(s) directly to optical depths.

- `ac2od` integrate absorption coefficients along the line-of-sight through atmosphere
- ......

All these scripts read their input from external files, and save their results on files, too, see the workflow indicated in Fig. 8. As a consequence, I/O operations can become quite time consuming (as the number of spectral grid points can become quite big); Furthermore a large part of the scripts was devoted to check the consistency of the various input files (e.g., the `xs2ac` script had to test that the different cross section files cover the same spectral range (or at least a common subset) for the same altitude range etc.) On the other hand, circumventing/bypassing some of the intermediate files is straightforward, especially if one is mainly interested in the final optical depth, cf. Fig. 9:

- `lbl2od` compute line-by–line cross sections, combine to absorption coefficients, and integrate through the atmosphere

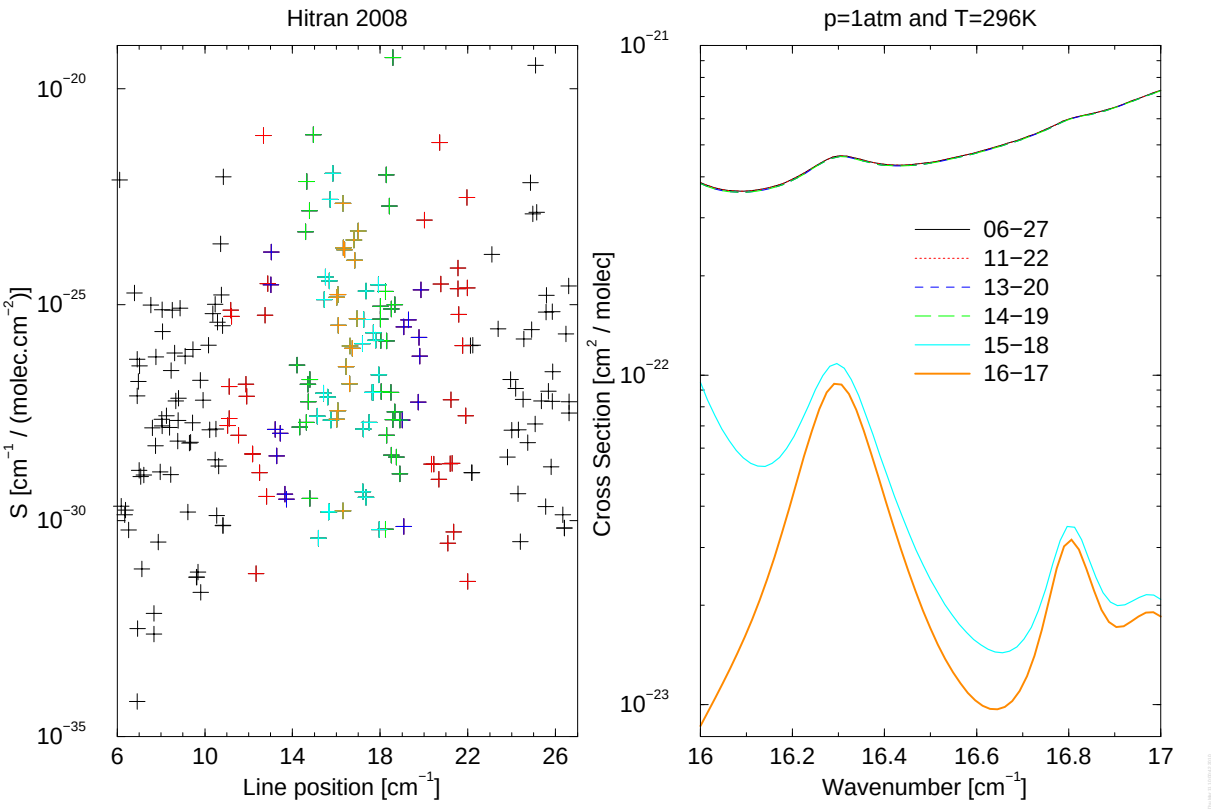

Figure 10: Impact of line wings on cross section in ODIN 501 GHz channel: H_2O.
A series of cross sections has been computed taking into account more and more lines to the left and right of the 16 – 17 cm^{-1} window.

5.1 Misc Remarks

Selection of spectral range, contributions from line wings
In order to compute cross sections, absorption coefficients, and optical depths for some spectral range $\nu_{\rm lo} \ldots \nu_{\rm hi}$, all lines in an extended spectral range $\nu_{\rm lo} - \delta \ldots \nu_{\rm hi} + \delta$ should be considered, where δ is typically some wavenumbers (cm^{-1}) (the actual size of δ depends on the number, density, and strengths of lines outside 'your' interval and on further factors such as pressure). As the `extract` and `lbl2od` (or `lbl2xs`) scripts are completely independent, this extension is not done automatically. The impact of line wing contributions on cross sections is demonstrated in Fig. 10.

References

M. Abramowitz and I.A. Stegun. *Handbook of Mathematical Functions*. National Bureau of Standards, AMS55, New York, 1964. 3.2

B.H. Armstrong. Spectrum line profiles: The Voigt function. *J. Quant. Spectrosc. & Radiat. Transfer*, 7:61–88, 1967. doi: 10.1016/0022-4073(67)90057-X. 3.2

S.A. Bühler, P. Eriksson, T. Kuhn, A. von Engeln, and C. Verdes. ARTS, the atmospheric radiative transfer simulator. *J. Quant. Spectrosc. & Radiat. Transfer*, 91:65–93, 2005. 1, 6

S.A. Clough and F.X. Kneizys. Convolution algorithm for the Lorentz function. *Appl. Opt.*, 18:2329–2333, 1979. doi: 10.1364/AO.18.002329. 3.1

S.A. Clough, F.X. Kneizys, G.P. Anderson, E.P. Shettle, J.H. Chetwynd, L.W. Abreu, L.A. Hall, and R.D. Worsham. FASCOD3: spectral simulation. In J. Lenoble and J.F. Geleyn, editors, *IRS'88: Current Problems in Atmospheric Radiation*, pages 372–375. A. Deepak Publishing, 1988. 1, 3.1, 5

P.F. Dubois and T.-Y. Yang. Extending Python with Fortran. *Computing in Science & Eng.*, 1(5):66–73, 1999. 5

D.P. Edwards. Atmospheric transmittance and radiance calculations using line–by–line computer models. In *Modelling of the Atmosphere*, volume 928, pages 94–116. Proc. SPIE, 1988. 1, 3.1

B.A. Fomin. Effective interpolation technique for line–by–line calculation of radiation absorption in gases. *J. Quant. Spectrosc. & Radiat. Transfer*, 53:663–669, 1995. 3.1

R.M. Goody and Y.L. Yung. *Atmospheric Radiation — Theoretical Basis*. Oxford University Press, second edition, 1989. 2.1

A.K. Hui, B.H. Armstrong, and A.A. Wray. Rapid computation of the Voigt and complex error functions. *J. Quant. Spectrosc. & Radiat. Transfer*, 19:509–516, 1978. doi: 10.1016/0022-4073(78)90019-5. 3.2, 3.2

J. Humlíček. An efficient method for evaluation of the complex probability function: the Voigt function and its derivatives. *J. Quant. Spectrosc. & Radiat. Transfer*, 21:309–313, 1979. doi: 10.1016/0022-4073(79)90062-1. 3.2

J. Humlíček. Optimized computation of the Voigt and complex probability function. *J. Quant. Spectrosc. & Radiat. Transfer*, 27:437–444, 1982. doi: 10.1016/0022-4073(82)90078-4. 3.2, 3.2

K. Imai, M. Suzuki, and C. Takahashi. Evaluation of Voigt algorithms for the ISS/JEM/ SMILES L2 data processing system. *Adv. Space Res.*, 45:669–675, 2010. doi: 10.1016/j.asr.2009.11.005. 3.2

N. Jacquinet-Husson, N.A. Scott, A. Chedin, L. Crepeau, R. Armante, V. Capelle, J. Orphal, A. Coustenis, C. Boonne, N. Poulet-Crovisier, A. Barbe, M. Birk, L.R. Brown, C. Camy-Peyret, C. Claveau, K. Chance, N. Christidis, C. Clerbaux, P.F. Coheur, V. Dana, L. Daumont, M.R. De Backer-Barilly, G. Di Lonardo, J.M. Flaud, A. Goldman, A. Hamdouni, M. Hess, M.D. Hurley, D. Jacquemart, I. Kleiner, P. Kopke, J.Y. Mandin, S. Massie, S. Mikhailenko, V. Nemtchinov, A. Nikitin, D. Newnham, A. Perrin, V.I. Perevalov, S. Pinnock, L. Regalia-Jarlot, C.P. Rinsland, A. Rublev, F. Schreier, L. Schult, K.M. Smith, S.A. Tashkun, J.L. Teffo, R.A. Toth, Vl.G. Tyuterev, J. Vander Auwera, P. Varanasi, and G. Wagner. The GEISA spectroscopic database: Current and future archive for Earth and planetary atmosphere studies. *J. Quant. Spectrosc. & Radiat. Transfer*, 109:1043–1059, 2008. doi: 10.1016/j.jqsrt.2007.12.015. 3.1

M. Kuntz. A new implementation of the Humlicek algorithm for the calculation of the Voigt profile function. *J. Quant. Spectrosc. & Radiat. Transfer*, 57:819–824, 1997. doi: 10.1016/S0022-4073(96)00162-8. 3.2

Hans Petter Langtangen. *Python Scripting for Computational Science*, volume 3 of *Texts in Computational Science and Engineering*. Springer, 2004. 1, 5

Kuo-Nan Liou. *An Introduction to Atmospheric Radiation*. Academic Press, Orlando, 1980. 2.1

C. Melsheimer, C. Verdes, S.A. Bühler, C. Emde, P. Eriksson, D.G. Feist, S. Ichizawa, V.O. John, Y. Kasai, G. Kopp, N. Koulev, T. Kuhn, O. Lemke, S. Ochiai, F. Schreier, T.R. Sreerekha, M. Suzuki, C. Takahashi, S. Tsujimaru, and J. Urban. Intercomparison of general purpose clear sky atmospheric radiative transfer models for the millimeter/submillimeter spectral range. *Radio Science*, 40:RS1007, 2005. doi: 10.1029/2004RS003110. 4.2

R.H. Norton and C.P. Rinsland. ATMOS data processing and science analysis methods. *Appl. Opt.*, 30:389–400, 1991. 2.2.1

J.J. Olivero and R.L. Longbothum. Empirical fits to the Voigt line width: a brief review. *J. Quant. Spectrosc. & Radiat. Transfer*, 17:233–236, 1977. doi: 10.1016/0022-4073(77)90161-3. 2.2.4

H.M. Pickett, R.L. Poynter, E.A. Cohen, M.L. Delitsky, J.C. Pearson, and H.S.P. Müller. Submillimeter, millimeter, and microwave spectral line catalog. *J. Quant. Spectrosc. & Radiat. Transfer*, 60:883–890, 1998. 3.1

L.S. Rothman, R.R. Gamache, A. Goldman, L.R. Brown, R.A. Toth, H.M. Pickett, P.L. Poynter, J.-M. Flaud, C. Camy-Peyret, A. Barbe, N. Husson, C.P. Rinsland, and M.A.H. Smith. The HITRAN database: 1986 edition. *Appl. Opt.*, 26:4058, 1987. 2.2.2

L.S. Rothman, I.E. Gordon, A. Barbe, D. Chris Benner, P.F. Bernath, M. Birk, V. Boudon, L.R. Brown, A. Campargue, J.-P. Champion, K. Chance, L.H. Coudert, V. Dana, V.M. Devi, S. Fally, J.-M. Flaud, R.R. Gamache, A. Goldman, D. Jacquemart, I. Kleiner, N. Lacome, W.J. Lafferty, J.-Y. Mandin, S.T. Massie, S.N. Mikhailenko, C.E. Miller, N. Moazzen-Ahmadi, O.V. Naumenko, A.V. Nikitin, J. Orphal, V.I. Perevalov, A. Perrin, A. Predoi-Cross, C.P. Rinsland, M. Rotger, M. Simecková, M.A.H. Smith, K. Sung, S.A. Tashkun, J. Tennyson, R.A. Toth, A.C. Vandaele, and J. Vander Auwera. The HITRAN 2008 molecular spectroscopic database. *J. Quant. Spectrosc. & Radiat. Transfer*, 110(9-10):533 – 572, 2009. doi: 10.1016/j.jqsrt.2009.02.013. 3.1

F. Schreier. The Voigt and complex error function: A comparison of computational methods. *J. Quant. Spectrosc. & Radiat. Transfer*, 48:743–762, 1992. doi: 10.1016/0022-4073(92)90139-U. 3.2

F. Schreier. Optimized evaluation of a large sum of functions using a three-grid approach. *Comp. Phys. Comm.*, 174:783–802, 2006. doi: 10.1016/j.cpc.2005.12.015. 3.3

F. Schreier. Optimized implementations of rational approximations for the Voigt and complex error function. *J. Quant. Spectrosc. & Radiat. Transfer*, 112(6):1010–1025, 2011. doi: 10.1016/j.jqsrt.2010.12.010. 3.2

L. Sparks. Efficient line–by–line calculation of absorption coefficients to high numerical accuracy. *J. Quant. Spectrosc. & Radiat. Transfer*, 57:631–650, 1997. doi: 10.1016/S0022-4073(96)00154-9. 3.1

G.P. Stiller, T. von Clarmann, B. Funke, N. Glatthor, F. Hase, M. Höpfner, and A. Linden. Sensitivity of trace gas abundances retrievals from infrared limb emission spectra to simplifying approximations in radiative transfer modelling. *J. Quant. Spectrosc. & Radiat. Transfer*, 72:249–280, 2002. 1, 5

A. Uchiyama. Line–by–line computation of the atmospheric absorption spectrum using the decomposed Voigt line shape. *J. Quant. Spectrosc. & Radiat. Transfer*, 47:521–532, 1992. 3.1

Thomas von Clarmann, M. Höpfner, B. Funke, M. López-Puertas, A. Dudhia, V. Jay, F. Schreier, M. Ridolfi, S. Ceccherini, B.J. Kerridge, J. Reburn, and R. Siddans. Modeling of atmospheric mid–infrared radiative transfer: The AMIL2DA algorithm intercomparison experiment. *J. Quant. Spectrosc. & Radiat. Transfer*, 78:381–407, 2002. doi: 10.1016/S0022-4073(02)00262-5. 4.1

J.A.C. Weideman. Computation of the complex error function. *SIAM J. Num. Anal.*, 31:1497–1518, 1994. doi: 10.1137/0731077. 3.2, 3.2

Wilford Zdunkowski, Thomas Trautmann, and Andreas Bott. *Radiation in the Atmosphere — A Course in Theoretical Meteorology.* Cambridge University Press, 2007. 2.1